Article

Effect of Cr Content on Corrosion Resistance of Low-Cr Alloy Steels Studied by Surface and Electrochemical Techniques

Alicja Łukaszczyk [1],*[iD]**, Jacek Banaś [1], Marcin Pisarek [2]**[iD]**, Antoine Seyeux [3], Philippe Marcus [3] and Jolanta Światowska [3],***[iD]

[1] Department of Chemistry and Corrosion of Metals, Faculty of Foundry Engineering, AGH University of Science and Technology, Reymonta 23, 30-059 Krakow, Poland; jbs@agh.edu.pl

[2] Institute of Physical Chemistry, Polish Academy of Sciences, Kasprzaka 44/52, 01-224 Warsaw, Poland; mpisarek@ichf.edu.pl

[3] Institut de Recherche de Chimie Paris, Chimie ParisTech—CNRS, PSL Research University, 11 rue Pierre et Marie Curie, 75005 Paris, France; antoine.seyeux@chimieparistech.psl.eu (A.S.); philippe.marcus@chimieparistech.psl.eu (P.M.)

* Correspondence: alicjal@agh.edu.pl (A.Ł.); jolanta.swiatowska@chimieparistech.psl.eu (J.Ś.)

Abstract: The electrochemical behavior of low alloyed Fe-Cr steels with 3 and 5% wt. of Cr in neutral Na_2SO_4 electrolyte combined with a detailed chemical and morphological characterization of these alloys performed by Auger electron spectroscopy, X-ray photoelectron spectroscopy, time-of-flight secondary ion mass spectrometry and scanning electron microscopy are presented here. The corrosion of low alloyed Fe-Cr steels proceeds in the prepassive range, with the formation of corrosion surface films having a duplex structure with outer iron oxide/hydroxide layer and inner Cr oxide-rich layer. The thickness, composition, and the morphology of the surface films vary as a function of chromium content in the alloy as well as conditions of electrochemical tests (temperature). Even a low chromium content shows a beneficial effect on the corrosion performances of the Fe-Cr steels. The chromium as a more active component than iron of ferrite increases the anodic activity of this phase, which results in a rapid saturation of the surface with the anodic reaction products forming a fine crystalline-like and compact layer of corrosion products. In this way, the chromium acts as a modifier of formation/crystallization of the iron-rich surface film (mainly magnetite) in the prepassive range.

Keywords: iron-chromium alloy; low Cr-alloy steel; oxide layer; XPS; ToF-SIMS; passivation

1. Introduction

Low- and medium-chromium steels are materials, which are commonly used in building constructions and industrial equipment. The application of these steels is related to their relatively good corrosion resistance in atmospheric conditions (weathering steels), in water and in steam at elevated temperatures [1–3]. Our previous studies on the corrosion of low-chromium steels at operating conditions in geothermal heating plants, as well as in laboratory experiments, revealed that the corrosion rate decreases nearly exponentially with the chromium content in the steel [4–8]. The results of Ueda et al. [9] show also exponential decay of corrosion rate of carbon steel with chromium content in aqueous solutions of carbonic acid and they were similar to date presented by Hua et al. [10].

The electrochemical laboratory tests, as well as the field tests, ruled out the possibility of passivation of low- and medium-chromium steel in thermal water at high temperatures (up to 150 °C) [5,7,8]. The electrochemical investigations of Fe-Cr alloys (containing from 1 to 5%Cr) and low-alloyed steels show that the corrosion of these materials in the H_2O-CO_2-H_2S system proceeds in the prepassive range [11]. Hitherto, the mechanism of the positive influence of chromium on the corrosion resistance of the low-alloyed steel has not been sufficiently investigated according to our knowledge. Two main explanations

of the positive effect of low chromium content on the enhanced corrosion resistance of carbon steel can be found in the literature. The first is related to the formation of spheroidal carbide from chromium as a carbide-forming element [12]. Then, the formed carbide facilitates the formation of a bainitic microstructure. This microstructure is characterized by a higher corrosion and abrasion resistance than the ferritic and martensitic one. Moreover, other than Cr alloys elements, such as Mo, Si, result in improved corrosion and abrasion properties.

The second explanation proposed by Cheng and Steward [13] shows that the positive influence of chromium is related to the enrichment of the surface film in Cr_2O_3 as a corrosion product. This thin film formed at the metal/film interface is responsible for a limited transport of electric charge, in comparison to the film containing only iron ions (Fe^{II}/Fe^{III}). Even a low content of chromium in steel (up to 2.5%) increases the rate of the surface film formation, which is beneficial for corrosion resistance. Xu et al. reported that the formation of protective $Cr(OH)_3$ layer, having a prepasivation characteristics, is responsible for the improved corrosion performance of low-Cr alloy steel [14]. The positive influence of low Cr content in steels was also demonstrated in atmospheric corrosion or corrosion under CO_2 environment [15,16]. The positive influence of the Cr on the corrosion performance has been widely studied for high chromium-content alloys [17–23]. A sufficiently high chromium content is decisive for their excellent passivating properties [24–27]. Many studies have shown that for less than 10% of Cr content, the properties of iron are dominating, whereas for more than 15%Cr content in the alloy, chromium has the major influence. Keller and Strehblow [28] have performed detailed XPS analysis on the surface layers formed on the Fe20Cr and Fe15Cr steels in the prepassive, passive, and transpassive potential range. These investigations performed on the layer formed in the prepassive range showed a formation of a homogeneous film composed of Cr(III) hydroxide and Cr(III) sulphate with a low quantity of Fe(II). In the passive range a bilayer structure can be formed: with the outer layer enriched in Fe or Cr hydroxides and with the inner part principally composed of Cr oxides. Iron exists only in a bivalent oxidation state. In the transpassive potential range a pronounced change of the layer composition was observed: with the outer part of the transpassive layer formed predominantly by Fe(III) species and with the inner part enriched in Cr_2O_3.

Based on thermodynamic diagrams (Fe-Cr-C-O-H), Inaba et al. [29] demonstrated that the increase of corrosion resistance of low chromium steels in humid CO_2 can be explained by the reduction of the Fe^{2+} stability range and formation of a $Fe_xCr_{3-x}O_4$ spinel. A small amount of chromium and copper in weathering construction steels lead also to the increase of the corrosion resistance under atmospheric conditions due to the formation of Cr_2O_3 and CuO_x phases in the first stages of corrosion [9,30]. Theses phases are therefore "modifiers" of the crystallization of the surface layer, consisting mostly of iron oxides/oxo-hydroxides. The formation of nanocrystalline structure of passive film on the polarized iron-chromium single crystal alloy was observed for the first time by STM [22]. The crystallized film was found to be more stable and corrosion resistant than the disordered film.

Temperature has also significant influence on mechanism of passivation, chemical composition, and structure of passive layer. At lower temperatures (under 50 °C), the growth of passive layer is limited by the high field mechanism [31]. At higher temperatures the growth of the oxide layer is limited by high electric field in the initial period of growth. After longer period of time the growth of oxide layer is determined by diffusion through the layer (decrease of electric field in the inner part of the layer as a result of an increase in the thickness of the oxide) [32,33].

The aim of this work is to present the influence of chromium on the corrosion resistance, morphology, and chemical composition of the corrosion products formed on low chromium (1, 3, and 5% of Cr) binary ferritic Fe-Cr alloys in Na_2SO_4 electrolyte as a function of temperature. The corrosion behavior was studied by electrochemical methods followed by chemical surface characterization by means of Auger and X-ray photoelectron spectroscopies (XPS) and time-of-flight secondary ion mass spectrometry (ToF-SIMS).

The morphologies of pristine and corroded samples were analyzed by scanning electron microscopy (SEM).

2. Experimental

2.1. Sample Preparation

Two types of samples were used in this study: a pure iron sample (Goodfellow with a purity of 99.999%) and a binary iron-chromium (Fe-Cr) alloy samples with different chromium contents of 1, 3, and 5%. To investigate the corrosion properties of this iron-chromium alloy with possibly the same homogenous ferritic microstructure, the samples were annealed at 1100 °C in Ar atmosphere. The composition of the examined alloys and annealing time are given in Table 1.

Table 1. Chemical composition (in wt%) of binary Fe-Cr alloys and time of annealing.

Alloy	C	Si	Mn	P	S	Cr	Ni	Mo	Cu	Annealing Time
Fe-1% Cr	0.03	0.01	0.131	0.012	0.011	0.87	0.019	<0.0007	0.0420	2 h
Fe-3% Cr	0.03	0.01	0.132	0.013	0.012	2.80	0.018	<0.0007	0.0366	50 h
Fe-5% Cr	0.03	0.03	0.126	0.021	0.015	5.16	0.020	<0.0012	0.0314	100 h

After the annealing, the specimens were mechanically ground with silicon carbide (SiC) emery papers down to 4000 grit, polished with diamond pastes down to 1 μm, and then washed with water and then ultrasonically rinsed in ethanol.

2.2. Electrochemical Measurements

The electrochemical measurements were performed in 0.1 M Na_2SO_4 (Reagent grade, Aldrich) at 20 °C, prepared with distilled water in a classical three-electrode cell, using a pure iron or Fe-Cr alloy sample (with surface of 0.5 cm^2) as the working electrode, a platinum wire as the auxiliary electrode, and a silver-silver chloride electrode (Ag/AgCl, 3M KCl) as the reference electrode. The measurements at higher temperatures (80 and 100 °C) were performed in autoclave at 20 MPa of Ar using an Ag/AgCl wire as the reference electrode. The values of the potentials were recalculated into the hydrogen scale (SHE-standard hydrogen electrode), taking into consideration the temperature coefficients. The measurements were conducted with the use of PGZ301 VoltaLab potentiostat in a solution deaerated with argon (at atmospheric pressure). The electrochemical investigations were performed by means of cyclic voltammetry (CV) or linear sweep voltammetry (LSV), and chronoamperometry measurements. The samples after chronoamperometry measurements performed at constant anodic potential were analyzed by surface sensitive techniques: AES, XPS, and ToF-SIMS.

2.3. Chemical and Morphological Characterization

After the electrochemical tests, the morphology and chemical composition of the Fe-Cr alloys were examined by means of a laser interference profilometry WYKO NT9300 of Veeco and a scanning electron microscope (SEM) Jeol 5500LV with an X-ray spectrometer EDS or WDS.

The surface chemical composition analysis was performed by high resolution scanning Auger microanalysis (AES) (VG Microlab 350, Thermo Electron Corporation, Beverly, MA, USA) and X-ray photoelectron spectroscopy (XPS) (VG ESCALAB 250, Thermo Electron Corporation).

AES spectroscopy combined with Ar$^+$ ion sputtering was used to measure the local chemical composition and depth profiles of the passive oxide layers. Discontinuous sputtering (5 s etching steps) was applied to gradually remove the oxide film. The sputtering parameters were: ion energy 3 keV, crater size 16 mm^2. The Auger spectra were recorded, after each sputtering period, at a primary energy $E = 10$ keV. The conversion of the Auger signals into an atomic concentration of the components was undertaken by using sensitivity

factors S_f from the Thermo VG Scientific database. Avantage software (version 3.44) was used for data acquisition and processing.

XPS analyses were carried out using an Al Kα monochromatized radiation m as an X-ray source. For all analyses, the take-off angle of the photoelectrons was 90°. Survey scans and high-resolution spectra (O 1s, C 1s, Fe 2p, Cr 2p) were recorded with pass energies of 100 and 20 eV, respectively. Data processing (peak fitting) was performed with the Avantage software (version 3.13) provided by Thermo Electron Corporation. The peaks were fitted using an asymmetric Gaussian/Lorentzian mixed function and Shirley background subtraction. Time-of-flight secondary ion mass spectrometry (ToF-SIMS) ion depth profile analysis was performed using a ToF-SIMS 5 spectrometer (IonToF). The spectrometer was run at an operating pressure of 10^{-9} mbar. A pulsed 25 keV Bi$^+$ primary ion source was employed for analysis, delivering 1.1 pA of current over a 100×100 μm^2 area. Depth profiling was performed by interlacing analysis with sputtering using a m Cs$^+$ sputter beam giving a 30 nA target current over a 500×500 μm^2 area. Negative ion profiles were recorded by reason of their higher sensitivity to fragments coming from oxide matrices.

3. Results and Discussion

3.1. Electrochemical Behavior of Pure Iron and Fe-Cr Alloys in 0.1 M Na$_2$SO$_4$ Solution

3.1.1. Electrochemical Behavior of Iron

The electrochemical properties of iron were studied by cyclic voltammetry (CV) in deaerated (by argon) 0.1M Na$_2$SO$_4$ solution. Figure 1a presents the influence of scan rate (1, 3, 5, and 10 V/min) on the CV curves performed at 20 °C. In the anodic region, two areas can be distinguished: one below the potential of about -0.6 V (area of *a1* peak), corresponding to the formation of the surface product Fe^{II} (FeO/Fe(OH)$_2$), and one above the potential, corresponding to the formation of the Fe^{II}/Fe^{III} layer (area of *a2* peak) (magnetite [34]). The latter is not a barrier film but a well-conducting film, thus a significant increase of the current density at potentials higher than -0.6 V, attributed to the anodic reaction occurring at the surface layer/alloy substrate interphase, can be observed. In the backward curve (Figure 1a) the peaks *c2* and *c1* correspond to the reduction of solid surface products such as magnetite and Fe^{II} compound, respectively.

From the relationship between peak current or peak potential and scan rate the reaction mechanism can be described such as formation of surface products and the process reversibility [35]. The linear dependence of the anodic current density i_{a1} as a function of scanning rate (Figure 1b) indicates that a non-equilibrium process occurs on the surface with the formation of the Fe^{II}-based film. The peak potential shifts to more positive values with the scan rate increase (linear dependence of the peak potential E_{a1} as a function of the scan rates [36], Figure 1c, which confirms the irreversibility of the anodic process).

The electrochemical behavior of pure iron and the effect of temperature (20, 80, and 100 °C) on its corrosion mechanisms in the prepassive range are presented in Figure 2a. At higher temperatures (80 and 100 °C) the increase of anodic current density related to iron oxidation (generalized corrosion) is moved to lower potentials. The formation and reduction of the surface anodic film at elevated temperatures is almost reversible.

The analysis of the fast polarization curves performed at high temperature (100 °C), shown in Figure 2b, demonstrates a Tafel anodic segment with the slope of 0.117 V/dec, corresponding to one reaction order with the formation of Fe(OH)$_2$ according to equation [37]:

$$\text{FeOH}_{ad} + \text{H}_2\text{O} \rightarrow [\text{Fe(OH)}_2]_{ad} + \text{H}^+ + \text{e} \tag{1}$$
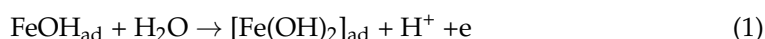
The backward curves performed at a high polarization rate (Figure 2c) show anodic segments with the slope from around 0.040 V/dec (for $v = 5$ V/min) to around 0.030 V/dec (for $v = 10$ V/min), which can correspond to the catalytic process of oxidation occurring on the surface with a small surface coverage by the FeOH$^+_{ad}$ intermediate product (Langmuir adsorption) [38].
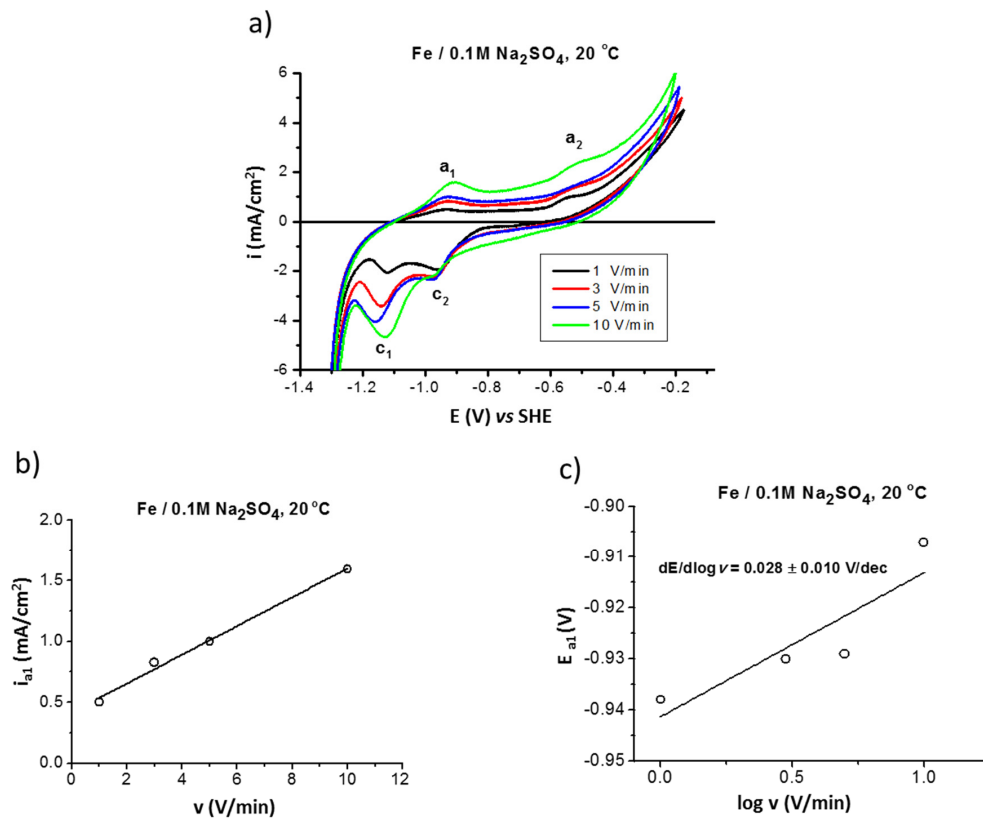
Figure 1. Polarization (CV) curves of iron in 0.1 M Na_2SO_4 saturated with argon at 20 °C performed at different scan rates v = 1, 3, 5, and 10 V/min (**a**); influence of scan rate on anodic current density i_{a1} (**b**); and on anodic peak potential E_{a1} (**c**).
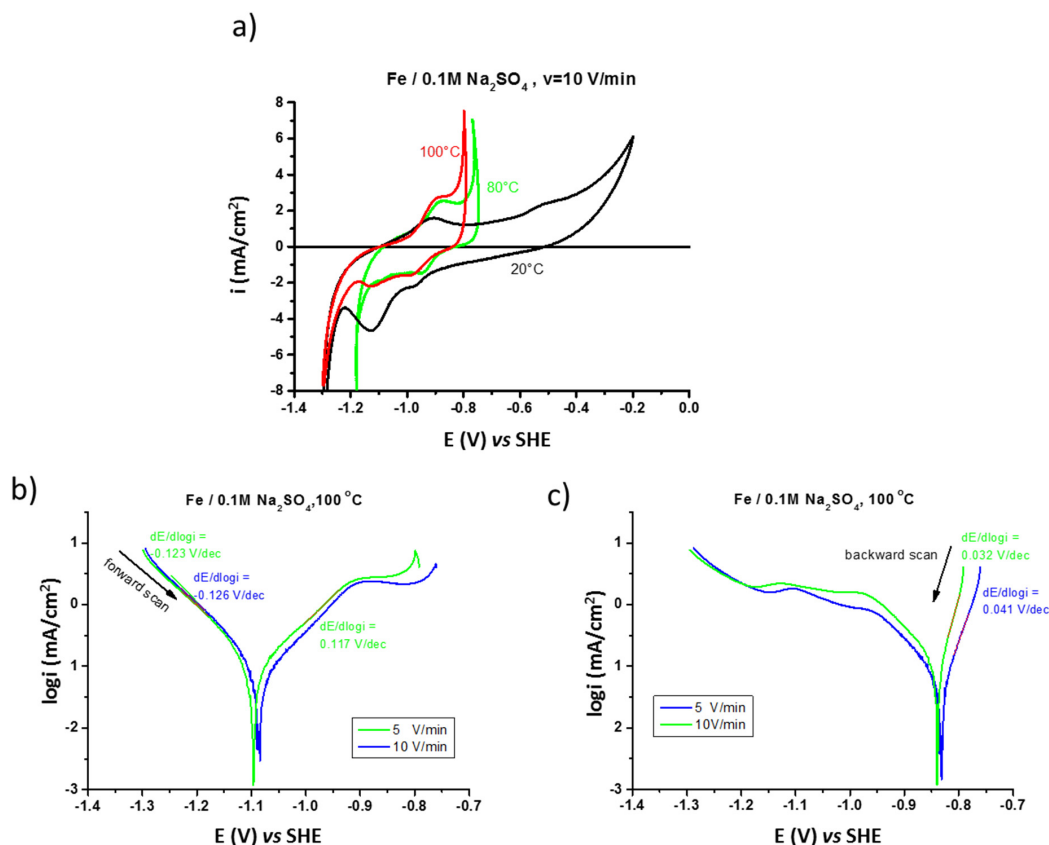
Figure 2. Influence of temperature on polarization (CV) of iron in 0.1 M Na_2SO_4 saturated with argon performed at v =10 V/min (**a**) fast polarization (v = 5 and 10 V/min) performed at 100 °C (**b**) forward, and (**c**) backward scans.

3.1.2. Electrochemical Behavior of Binary Fe-Cr Alloys

Figure 3 shows polarization curves performed on low chromium binary Fe-Cr alloys (with 1, 3, and 5% of Cr) in 0.1M Na_2SO_4 electrolyte deaerated with argon at 20 and 80 °C. In the region I, an increase of the anodic current (red arrow in Figure 3a) as a function of chromium content can be explained by fast dissolution of alloy, with the formation of thinner layer (with the surface compound $Fe(OH)_2$ formed at E vs. SHE < −0.7 V). At higher potentials, the region II (E vs. SHE > −0.7 V) corresponds to the formation of barrier, magnetite-like layer (oxidation of $Fe(OH)_2$ into Fe_3O_4) enriched in chromium compounds. The increased stability of this barrier layer as a function of the higher chromium content can be evidenced by the displacement of the current density increase to higher potentials (marked by green arrow): −0.68 V for the Fe-1% Cr, −0.55 V for the Fe-3% Cr, and −0.31 V for the Fe-5% Cr.
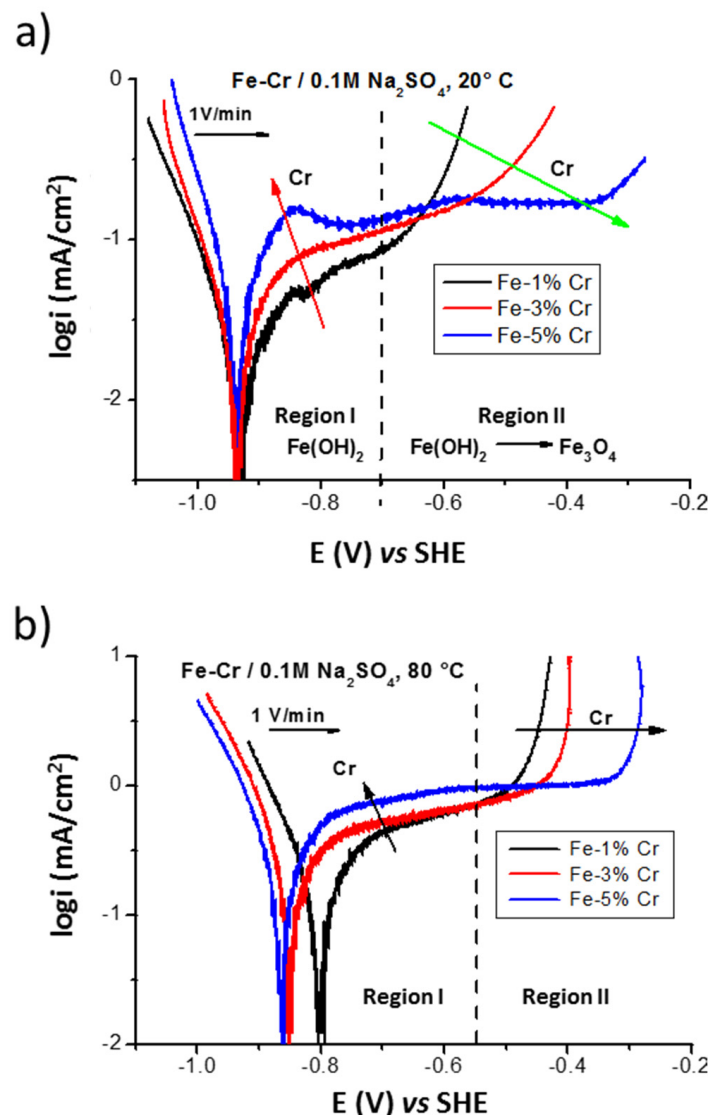
Figure 3. The influence of the chromium content on the polarization of the Fe-Cr ferritic alloys in 0.1 M Na_2SO_4 performed with scan rate $v = 1$ V/min at 20 °C (**a**) and 80 °C (**b**).

At higher temperatures (at 80 °C, Figure 3b) a slightly higher current density (around one order of magnitude) of the plateau can be observed in the region I, which can be explained by a thinner surface film formation and less corrosion resistant than those formed at 20 °C (Figure 3a). In the region II (above −0.55 V) the similar tendency can be

observed as for the results obtained at 20 °C with the beneficial effect of corrosion behavior for alloys with higher chromium content.

In order to determine the effect of chromium on the formation of the anodic surface layer, chronoamperometry measurements were performed at a constant potential (at *E* vs. SHE = −0.5 V) (Figure 4). A higher chromium amount (5% Cr) significantly increases the rate of the anodic reaction in the first few seconds, which is consistent with the higher current density of the plateau in the region I (Figure 3). However, after a longer time (~15 s) of exposure at 20 °C, a current decrease (almost 7 times lower for Fe-5%Cr than for Fe-1%Cr) can be observed. At 80 °C, a higher discrepancy (almost 10 times) between the current densities for both samples can be observed. The higher anodic dissolution of Fe-5%Cr alloy in the first seconds of polarization leads to more rapid nucleation of the surface product due to higher chromium content, which leads to a faster saturation of surface anodic product. The rapid nucleation, enhanced by higher chromium content, results in the formation of a more uniform, crystalline-like layer of corrosion product (magnetite-like) [22], and/or more complex and stable spinel compound $Fe_xCr_{3-x}O_4$ [29] on Fe-5%Cr than on the Fe-1%Cr. Therefore, this layer shows better barrier properties during the long time exposure. The higher temperature leads also to faster formation of surface products and stabilization of current density (5 s vs. 15 s for 20 and 80 °C, respectively).
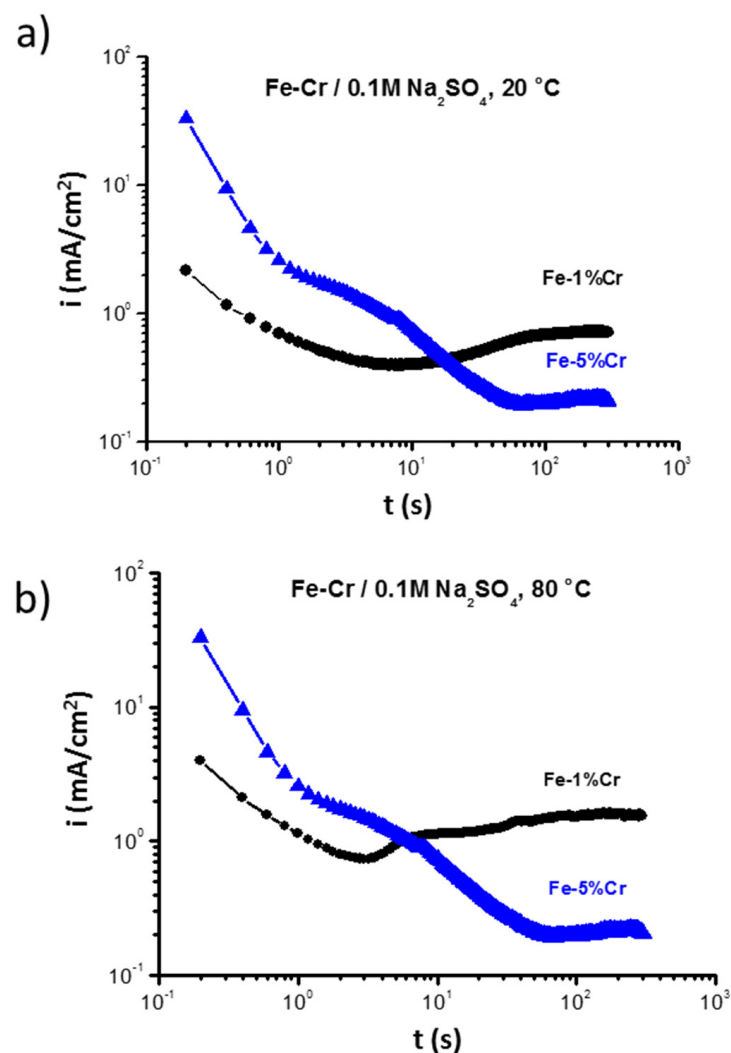
Figure 4. Chronoamperometry measurement performed for Fe-1%Cr and Fe-5%Cr at a constant potential (*E* vs. SHE = −0.5V) in 0.1M Na_2SO_4 at (**a**) 20 °C and (**b**) 80 °C.

3.2. Morphological and Chemical Characterization of Binary Fe-Cr Alloys before and after Electrochemical Test

3.2.1. Morphological Characterization

The formation of a more uniform layer on the alloy with higher chromium content (5%) was confirmed from analysis of surface morphology by means of laser profilometer and a scanning electron microscope (Figure 5) performed after chronoamperometric measurements at a potential corresponding to the prepassive region. As it can be observed by profilometer images (Figure 5a,b), the rough surface layer (Z variation from -3.5 to 4.6 µm for Fe-1%Cr or -4.5 to 6 µm for Fe-3% Cr) formed on the surface of the alloy containing 1% and 3% Cr is composed of big particles and/or grains (of few tens of micrometers) randomly distributed. The sample with 5% of Cr content (Figure 5c) can be characterized by the formation of a relatively smooth surface layer (variation in Z from -1.3 to 0.8 µm) without any specific features, which can be attributed to different layer composition as evidenced by the XPS and ToF-SIMS characterizations presented hereafter. The SEM confirms the homogenous layer formed on the Fe-5% Cr alloy (Figure 5f). For the lower (1 and 3%) chromium content alloys (Figure 5d,e), the surface layer is built of grains and flakes. Moreover, this layer (for 1% and 3% of Cr content alloys) does not cover homogenously the alloy surface and numerous cracks can be observed. The formation of layers with several surface defects (irregular grains, particles, and cracks) can be a reason of lower corrosion performance as aforementioned.
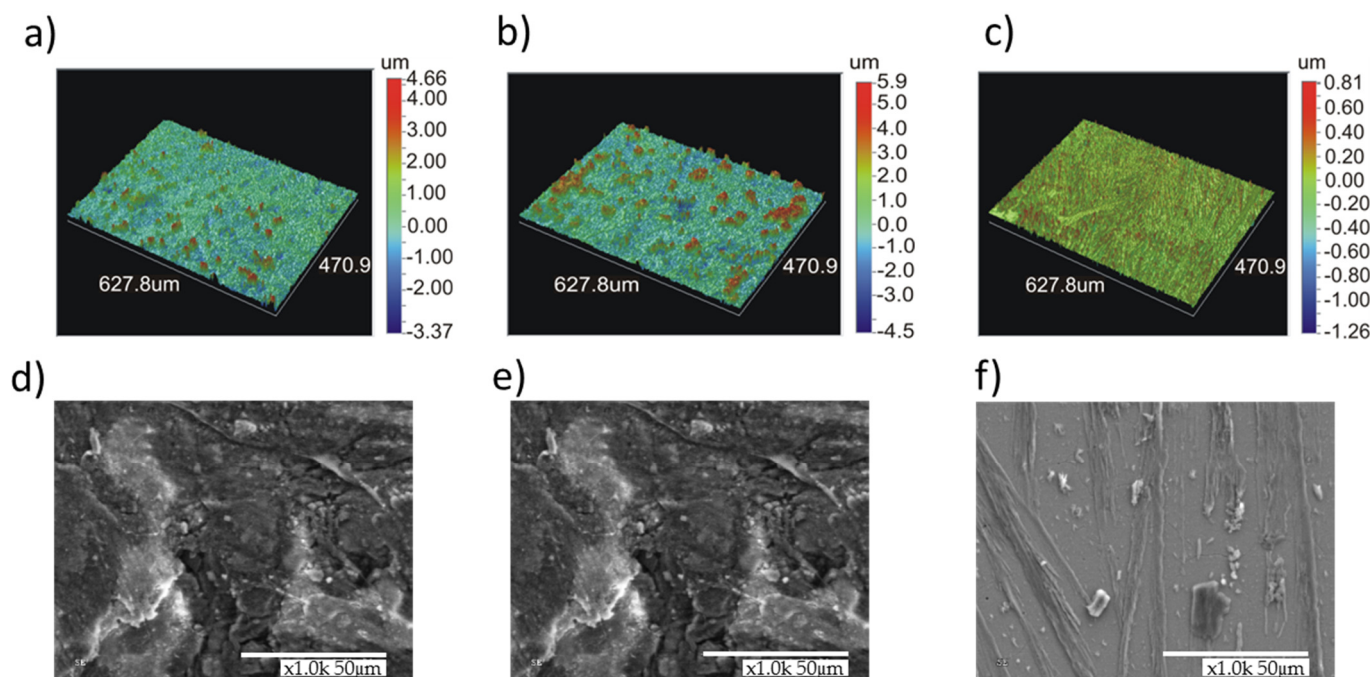
Figure 5. Surface morphology images performed by a laser profilometer and SEM images of Fe-1% Cr (**a,d**), Fe-3% Cr (**b,e**) and Fe-5% Cr (**c,f**) alloys after chronoamperometric measurements at a constant potential (*E* vs. SHE = -0.5 V) in 0.1 M Na$_2$SO$_4$ at 80 °C.

3.2.2. AES and XPS Analysis of Surface Layer of Binary Fe-Cr Alloys

Figure 6 presents the typical Auger spectra taken locally (lateral resolution ~25 nm) at the surface of investigated alloys after chronoamperometry at a constant potential -0.7 V, corresponding to the prepassive region. All spectra revealed that the oxide layers are enriched in Fe and O. For the alloy with the 1% Cr content (Figure 6a) no chromium signal was detected. However, Cr signals were detected for the Fe-3%Cr (Figure 6b) and Fe-5%Cr alloys (Figure 6c) after 10 s or 20 s of sample sputtering by argon ion gun, respectively. This

kind of careful etching (ion energy 3 keV, crater size 36 mm^2) was used to remove carbon contamination present on the extreme surface (the first few nanometers).
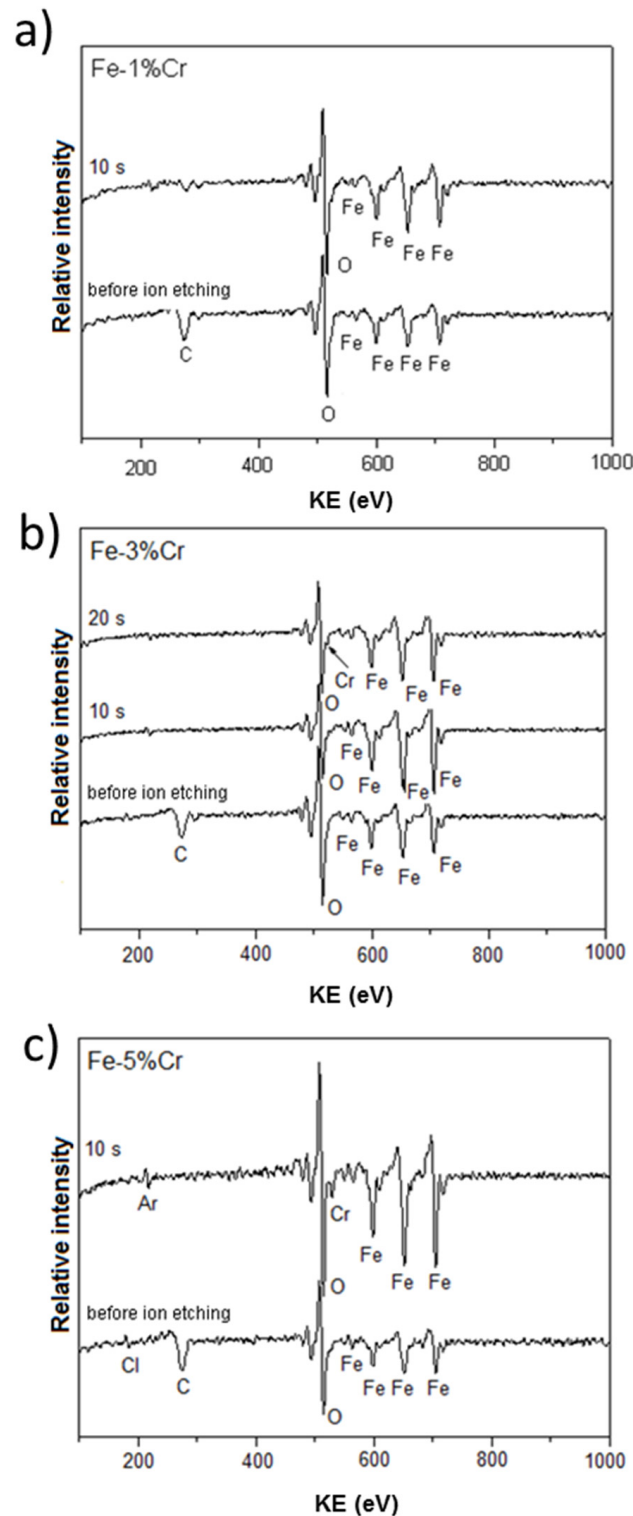
Figure 6. AES analysis of the chemical composition of Fe-Cr alloys ((**a**) 1%, (**b**) 3%, and (**c**) 5% of Cr) after chronoamperometric measurements at a constant potential (*E* vs. SHE = −0.7V) in 0.1 M Na$_2$SO$_4$ at 80 °C.

The element distribution profiles with the exception of chromium in the oxide layers on the surface of alloys Fe-3% Cr and Fe-5% Cr are very similar. The chromium content in

the anodic layer on alloy Fe-3% Cr is much lower than that in the layer on the alloy with 5% Cr and it is in the limit of detection (so the depth profile is present only for Fe-5% Cr alloy). As seen from the depth profile (Figure 7), the oxide layer formed on the Fe-5%Cr, was removed after ~20 s of sputtering (ion energy 3 keV, crater size 16 mm^2). Two zones can be clearly distinguished in the profile: one corresponding to the oxide layer with a small amount of chromium which significantly increases after 15 s of argon sputtering and reaches the intensity corresponding to about 3% at. and a second one related to a metallic alloy substrate containing mostly iron and chromium. These results suggest that the presence of chromium in the inner part of the oxide layer contributes to the growth of the crystallization nuclei of the oxide phase.
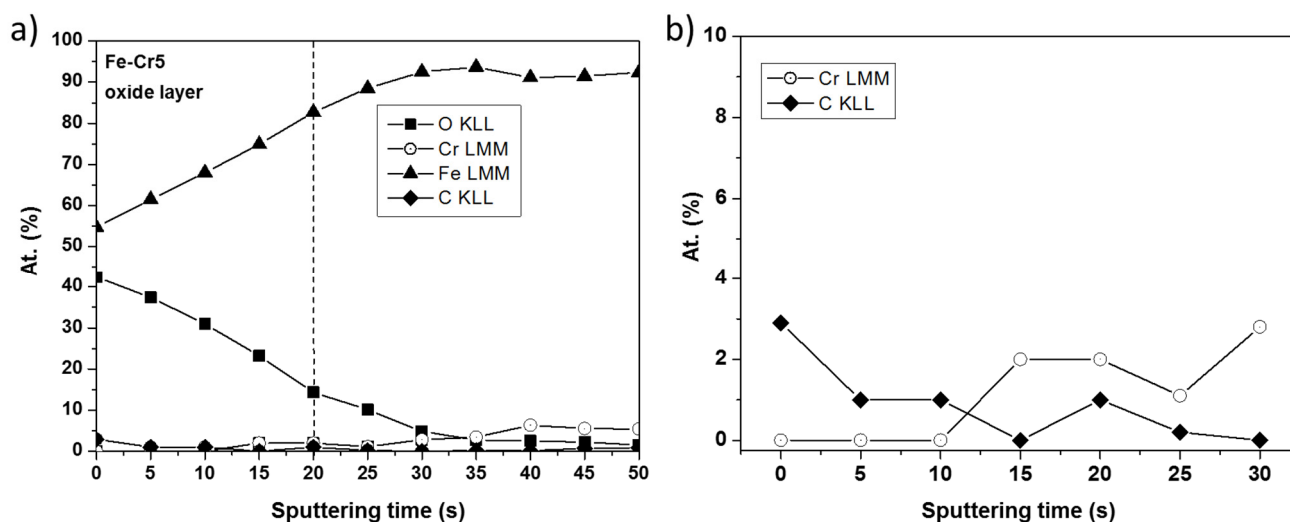
Figure 7. Distribution of elements Fe, Cr, O, C in anodic layer formed on alloy Fe-5% Cr after chronoamperometric measurements: (**a**) the full sputtered thickness, (**b**) the sputtered thickness corresponding principally to the oxide layer.

Hereafter, a detailed XPS surface analysis is presented for pristine samples and after sample polarization at constant potential. Figure 8 presents the XPS spectra of the Fe-5% Cr pristine sample. The O 1s peak (Figure 8a) was decomposed into three components at O 1s = 530.7 eV (*FWHM* = 1.2 eV), O 1s =532.1 eV (*FWHM* = 1.6 eV), and O 1s = 533.6 eV (*FWHM* = 1.7 eV), which can be ascribed to iron or chromium oxides, hydroxides [39–41] and molecular water, respectively. The two peaks corresponding to hydroxide (O 1s) and molecular water (O 1s) can overlap with the small intensity peaks assigned to contaminations, namely O–C=O.

The contaminations are observed in the region of C 1s core level (Figure 8b), namely C 1s at 286.7 eV (*FWHM* = 1.6 eV) and C 1s peak at 289.0 eV (*FWHM* = 1.7 eV) ascribed to C–O and O–C=O [42], respectively. The main carbon peak set at C 1s = 285.0 eV is assigned to hydrocarbons, –CH$_2$CH$_2$–, always detected at the extreme surface. The small intensity C 1s peak at lower binding C 1s = 282.7 eV (*FWHM* = 1.0 eV) can be ascribed to small quantity of iron carbide Fe$_3$C [43].

Decomposition of the Fe 2p$_{3/2}$ peaks (Figure 8c) was performed according to previous analysis and calculation made by Gupta and Sen [44,45] and investigation of multiplet splitting of Fe 2p XPS spectra performed by Grosvenor et al. [46]. The 2p$_{3/2}$ peak for high-spin Fe^{3+} and Fe^{2+} compounds is broadened compared to Fe^0 metal or low-spin Fe^{2+} [47]. The broadness of these peaks, shown already by Gupta and Sen (GS) [44,45] is due to the inclusion of electrostatic interactions, spin-orbit coupling between the 2p core hole and unpaired 3d electrons of the photoionized Fe cation and crystal field interactions.
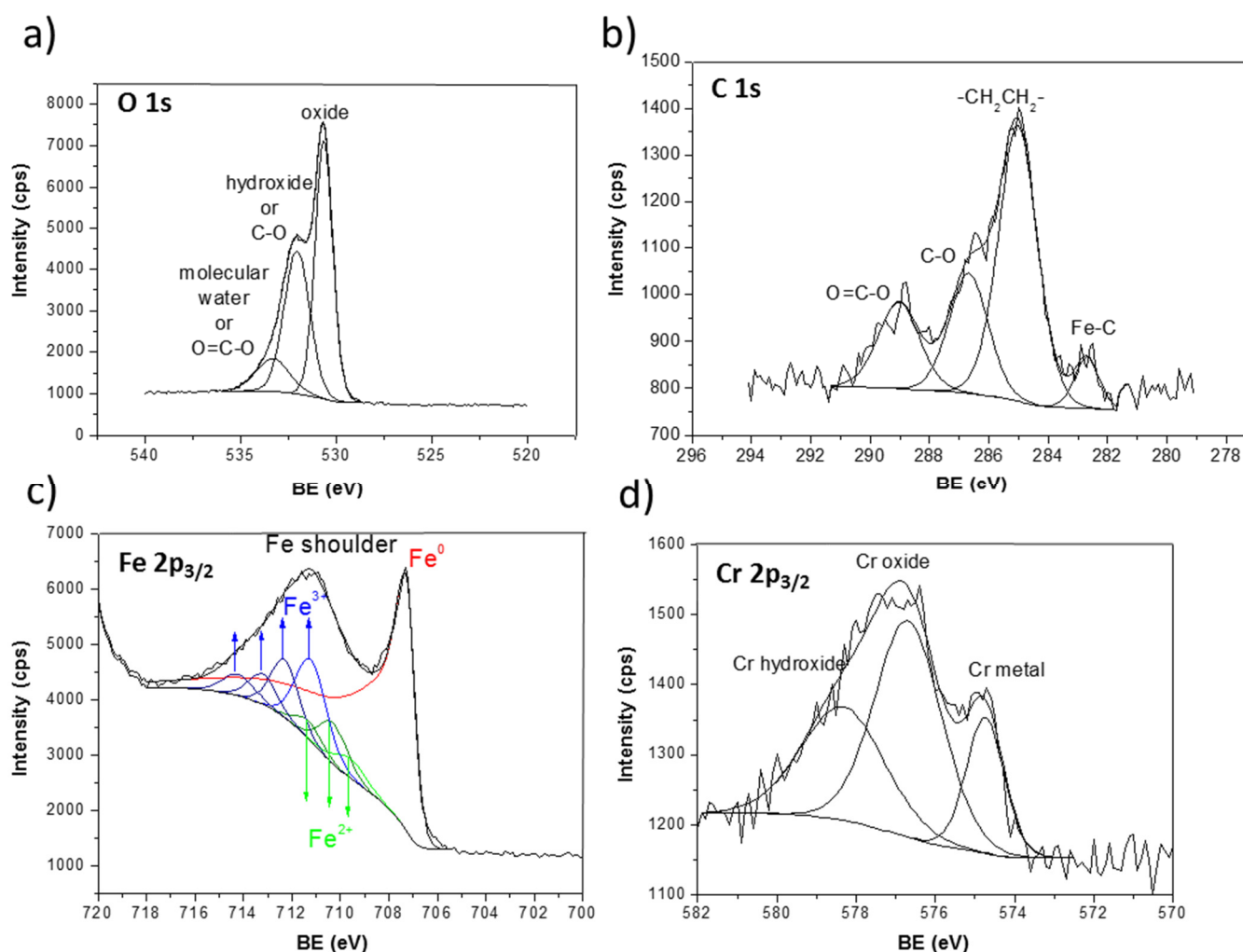
Figure 8. XP spectra for Fe-5% Cr pristine sample (**a**) O 1s, (**b**) C 1s, (**c**) Fe 2p, (**d**) Cr 2p.

A metal component at 707.3 eV (*FWHM* = 1.7 eV) appears in the spectrum for both Cr-Fe alloys (here shown only a detailed decomposition for Fe-5% Cr alloys in Figure 8). In this study, it was found that the Fe $2p_{3/2}$ spectrum was well fit using the GS multiplets for both the Fe^{2+} and Fe^{3+} components labelled in Figure 8. The presence of overlapping multiplets made it difficult to separate the two phases, but the intensities found for the Fe^{3+} and Fe^{2+} multiplets correspond well to those found also by Grosvenor et al. [46]. The three peaks (marked as Fe^{2+} in Figure 8c) found at binding energy of 709.6, 710.3, and 711.3 eV (with *FWHM* of around 1.5 ± 0.1 eV) can be assigned to Fe^{2+} in Fe_3O_4 and/or FeO [46]. The four higher binging energy peaks at 711.2, 712.3, 713.2, and 714.21 eV (with *FWHM* ~1.5 ± 0.1 eV) correspond to Fe_2O_3 [46]. However, the presence of FeOOH on the surface of Fe-5% Cr alloys, which can be found at slightly higher binding energy as Fe_2O_3 compound (of around >0.5 eV), cannot be excluded. The presence of iron and/or chromium hydroxides has already been confirmed from the contribution of OH peak in O 1s core level spectra.

The Cr $2p_{3/2}$ spectra presented in Figure 8d were decomposed into three peaks located at 574.7, 576.7, and 578.3 eV, which can be attributed to metallic chromium, Cr_2O_3 and $Cr(OH)_3$ [48–52].

The surface analysis of the Fe-1%Cr pristine alloy shows the same chemical composition. The principal difference between these two alloys is mainly the lower quantity of chromium compounds (oxides and hydroxides) present in the native oxide layer formed on the surface of the Fe-1% Cr pristine sample.

The polarization of both alloys significantly modifies the composition of the surface layers. Figure 9 shows the comparisons of Cr 2p and Fe 2p core level spectra obtained

for pristine samples and after the CA measurements at 20 and 80 °C for Fe-1% Cr (a) and Fe-5% Cr (b) alloys. In a case of low quantity of chromium in alloy (Fe-1% Cr) a thin and/or not homogenous, rough layer with presence of defects is formed after sample polarization at 20 °C. The formation of this layer with lots of defects (i.e., cracks) was already confirmed by SEM measurements presented above. The composition of this layer seems to be almost similar to the native oxide layer which can be deduced from the presence of metallic iron visible at low binding energy (Figure 9a), Fe 2p spectra after CA @ 20 °C. Only slightly more intense the Fe 2p as well as the Cr 2p peak (Figure 9a) corresponding to oxides and hydroxides indicates a slight increase of thickness of this layer formed in the prepassive region when comparing to native oxide layer present on the pristine sample. The polarization of Fe 1% Cr samples at higher temperature (80 °C) leads to uptake of the anodic surface layer, which can be concluded from a complete attenuation of Fe metallic peak and presence of iron oxides/hydroxides. High intensity of Cr 2p peak indicates enrichment of anodic/corrosion layer in Cr-like components (mainly Cr_2O_3 and $Cr(OH)_3$). The enrichment of the anodic layer in chromium when comparing to quantity of chromium present in the native oxide layer or the bulk material, has already been observed for higher Cr content Fe-Cr alloys [17,53–55]. The presence of both iron and chromium oxides can indicate a formation of spinel compound $Fe_xCr_{3-x}O_4$ [29].
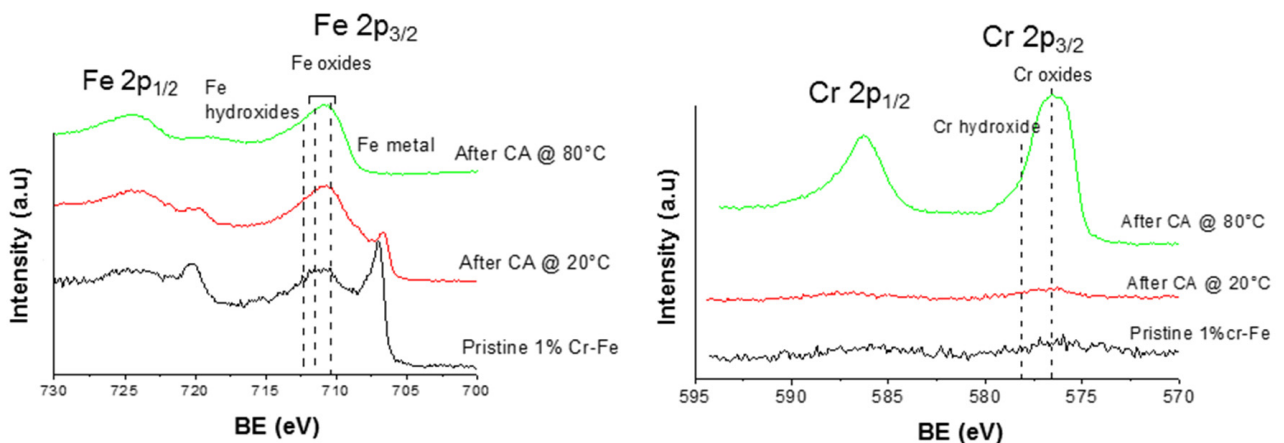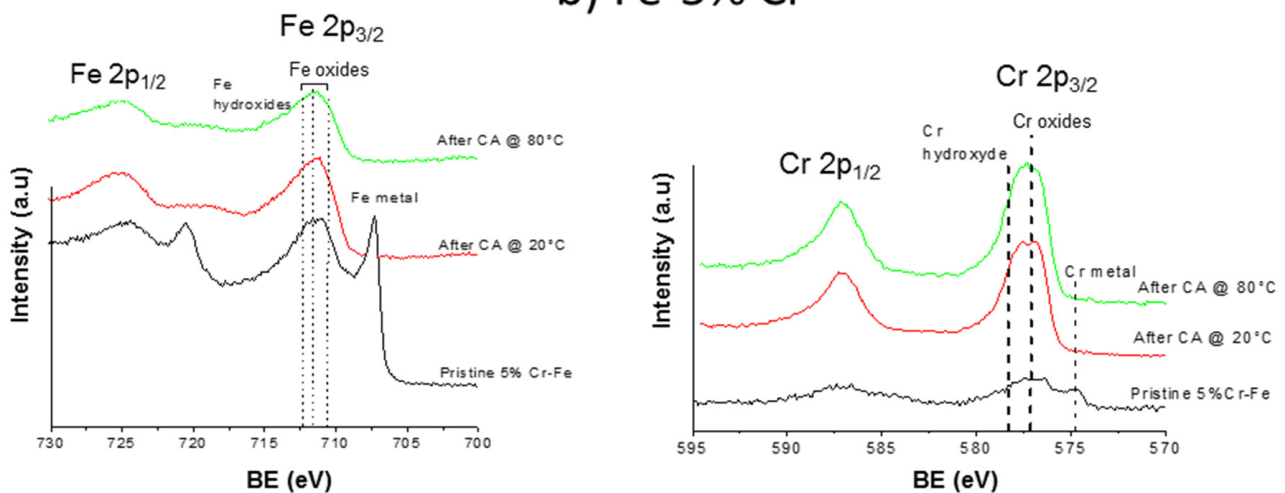
Figure 9. Comparison of Fe 2p and Cr 2p spectra for Fe-1% Cr (**a**) and Fe-5% Cr (**b**) performed for pristine samples and after chronoamperometric measurements in passive region at 20 °C and 80 °C.

Different behavior can be observed for the alloy containing higher chromium content (Fe-5% Cr, Figure 9b). Already after polarization at 20 °C the complete attenuation of metallic iron and chromium can be observed, indicating the formation of thick anodic layer (with the thickness higher than analysis depth of XPS around 10 nm). The composition of this anodic layer seems to be stable with the principal components of iron and chromium oxides/hydroxides. The polarization at higher temperature (80 °C) does not influence the layer composition when comparing to the film formed at lower temperature (20 °C). From the XPS results presented above it can be concluded that the higher quantity of chromium in the alloy leads to the formation of thick and/or homogenous protective, anodic layer after polarization (CA measurements) already at 20 °C. This layer is much richer in chromium (mainly chromium oxides) when compared to thin native oxide layer. In contrary, in the same experimental conditions, the layer does not cover the surface of Fe-1% Cr sample. The polarization at higher temperatures seems to cover homogenously, the both alloys leading to high enrichment of the surface layer in chromium. The XPS results are in agreement with the electrochemical results showing better corrosion behavior and the results obtained from profilometry and SEM analyses showing more smooth and homogenous film formation in case of Fe-Cr alloys richer in Cr content.

3.2.3. ToF-SIMS—Surface and Bulk Modifications Layers Formed on the Binary Fe-Cr Alloys

ToF-SIMS negative ion depth profiling was performed for both alloys in order to investigate the chemical surface and bulk composition of native oxides and anodic layers formed after polarization (CA measurements) performed in the prepassive region. Figure 10 shows the ToF-SIMS negative ion depth profiles for the pristine Fe-1%Cr and Fe-5%Cr samples. Note that the intensity is reported using a logarithmic scale, which emphasizes the low intensity signals. The variation of the ion intensity with sputter time reflects the variation of the in-depth concentration but it is also dependent on the matrix, from which the ions are emitted. Several regions can be identified. The first few seconds (13–15 s) of sputtering with small carbon and hydroxide peaks in the C^- and OH^- ion profiles, correspond to a very thin surface contamination film. The presence of contamination and hydroxide layer on the surface of both samples have been already confirmed by XPS analysis. The presence of surface hydroxide layer has been observed previously [17]. Then, a stable intensity of the FeO_2^- and O_{18}^- signals can be characteristic of the presence of a native oxide layer on the Cr-Fe alloy substrates. The width of a plateau corresponding to this oxide is slightly larger for the pristine sample with a higher chromium content, which can indicate a slightly thicker layer. The higher chromium content in the Fe-5% Cr alloys is clearly visible by the higher intensity of the Cr^- and CrO^- ion profiles both in the region of the native oxide layer and in the bulk of alloy substrate (Figure 10a,b), which also corroborates with the AES (Figure 6) and XPS results (Figure 9b). The intensities of both ion profiles (Cr^- and CrO^-) in the region corresponding to the native oxide increase with sputtering time, which indicates that the inner part of the native oxide at the native oxide/alloys substrate interface is enriched in the chromium oxides. From the ToF-SIMS profiles (a stable intensity of FeO_2^- profile) it can be concluded that the outer part of the native oxide layer is rich in iron oxides. These results clearly show a duplex structure of the native oxide layer present on the low chromium-content alloys, which is composed of the outer (iron-rich oxide layer) and inner (chromium-rich oxide) layers. The enrichment of the oxide layer in the chromium oxides increasing with sputtering time can be easily observed in Figure 11 from the intensity ratio of CrO^-/FeO_2^- signals. The increase of some other ion profile intensities (C^-, $FeOH^-$, and OH^-), in the area of the native oxide/alloy substrate interfacial region indicates a higher concentration of contaminants and hydroxides. The matrix modifications and different sputtering yields in this transition region between native oxide and alloy substrate resulting in higher ion intensities cannot be completely ruled out.
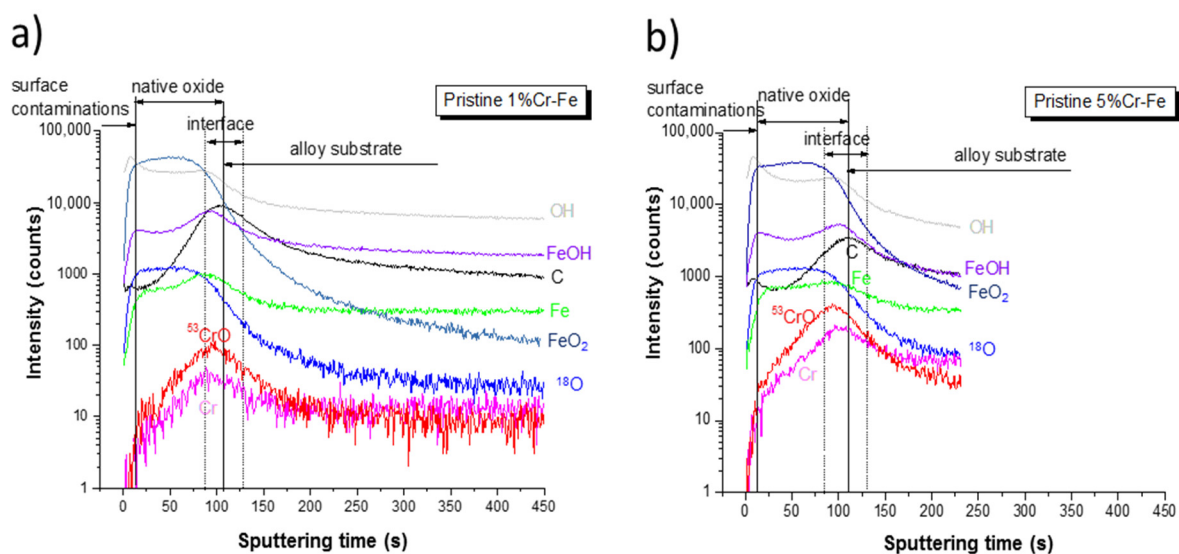
Figure 10. ToF-SIMS negative ion depth profiles for the (**a**) Fe-1% Cr and (**b**) Fe-5% Cr pristine samples.
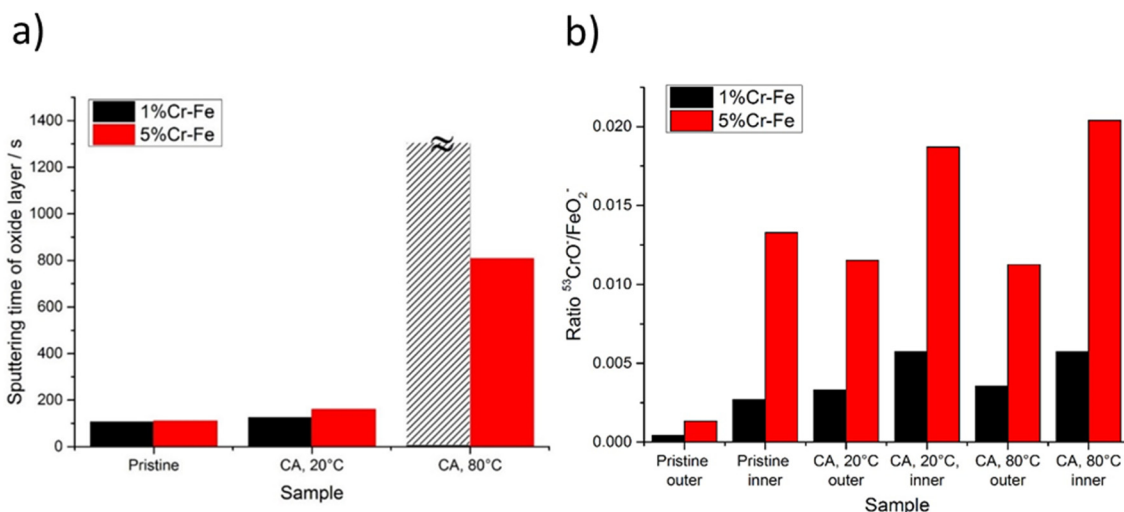
Figure 11. (**a**) ToF-SIMS sputtering time corresponding to thickness of the oxide layer for pristine samples and after polarization (chronoamperometric measurements) for 1% and Fe-5% Cr alloys; (**b**) ToF-SIMS CrO^-/FeO_2^- intensity signal ratio for pristine sample and after polarization for 1% and Fe-5% Cr alloy samples measured in the beginning of sputtering time (outer layer) and at the oxide/alloy substrate interface (inner layer).

The significant modifications of ion depth profiles (Figure 12) can be observed after polarization (CA measurements) performed on both alloys already at 20 °C. The anodic films formed on the surface of aged alloys show modified chemical composition and thickness (Figure 12). A slight increase of the surface film thickness (marked as "passive layer increase" in Figure 12) can be observed after aging at 20 °C in comparison to pristine samples (Figure 10). The 5%Cr alloy shows thicker layer than those observed on the Fe-1% Cr alloy (Figure 12). However, a temperature increase up to 80 °C results in a significant increase of surface layer thickness, which can be deduced from much higher (~808 s for 5%Cr-Fe, 80 °C) sputtering time as compared to the Fe-5% Cr polarized at 20 °C (160 s). For the Fe-1% Cr sample after polarization performed at 80 °C it is very difficult to define the thickness of the surface layer due to a stable intensity of ion signals. It can indicate the enhanced formation of layer built of corrosion products composed of Fe-like species and lower quantity of Cr-species than those observed on Fe-5% Cr sample. Thus, it can be concluded that 1% of chromium content in the alloy is not enough to efficiently protect the substrate against corrosion in these corrosive conditions.
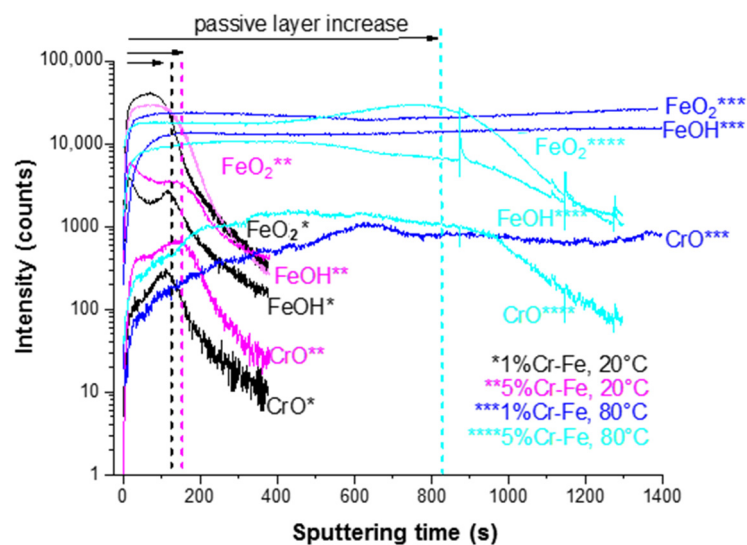
Figure 12. ToF-SIMS negative ion depth profiles for the Fe-1% Cr and Fe-5% Cr samples after polarization (chronoamperometric measurements) at 20 and 80 °C.

The composition of the oxide layer varies as a function of the electrochemical treatment (Figure 11b). A linear increase of the chromium oxide content (represented by higher CrO^-/FeO_2^- ratio) can be observed in the inner part of the oxide for the Fe-5% Cr alloy. The composition of the outer part is more stable as a function of temperature increase. For the Fe-1% Cr alloy the most significant modifications can be observed between pristine sample and sample after CA measurements. The temperature increase from 20 to 80 °C has no significant influence on the composition of inner and/or outer part of the oxide.

4. Conclusions

The corrosion potential of iron and low-chromium Fe-Cr alloys in neutral aqueous solutions is located within the range of potentials corresponding to the transformation $Fe(OH)_2 \rightarrow Fe_3O_4$. The barrier properties of the film Fe^{II}/Fe^{III} containing some chromium oxides determine the corrosion resistance of the low chromium Fe-Cr alloys in neutral Na_2SO_4 electrolytes.

The surface analysis of the low-chromium Fe-Cr alloys polarized in neutral aqueous solutions of Na_2SO_4 showed the enrichment of the anodic layer of corrosion products in chromium as shown by AES, XPS, and ToF-SIMS analyses. This Cr-enrichment is more significant in the inner part of the layer as evidenced by ToF-SIMS depth profiling and Auger elemental depth profile. The anodic film obtained on the alloy surface by chronoamperometric measurements is composed of iron oxides (Fe_3O_4, Fe_2O_3) and chromium oxide Cr_2O_3 and small quantity of hydroxides (FeOOH and $Cr(OH)_3$) present on the extreme surface.

The positive effect of chromium cannot be explained by the passivation of the steel surface caused by the chromium-rich oxide film, which is formed as a result of the direct surface reaction (*solid state reaction*)—as it was the case of the passivation of high-chromium alloy steels. In the case of low-chromium steels, the presence of chromium increases the anodic activity of the ferrite as observed by electrochemical measurements at lower anodic potentials. This increase of anodic activity for steels with higher Cr content (5%) results in a rapid oversaturation of the surface into an anodic product. This leads to an enhanced formation of a fine-crystalline and homogenous layer of corrosion products of the $M^{II}O/M^{III}_2O_3$ type. The protective properties of this film increases with the increase of the chromium content in the alloy.

Author Contributions: Conceptualization, J.B., A.Ł. and J.Ś.; methodology, A.Ł. and J.Ś.; validation, P.M., M.P., J.B. and A.S.; formal analysis, M.P., A.S.; investigation, A.Ł.; resources, A.Ł.; data curation,

References

1. Brownlie, F.; Hodgkiess, T.; Pearson, A.; Galloway, A.M. A study on the erosion-corrosion behaviour of engineering materials used in the geothermal industry. *Wear* **2021**, *477*, 203821. [CrossRef]
2. Sun, M.; Du, C.; Liu, Z.; Liu, C.; Li, X.; Wu, Y. Fundamental understanding on the effect of Cr on corrosion resistance of weathering steel in simulated tropical marine atmosphere. *Corros. Sci.* **2021**, *186*, 109427. [CrossRef]
3. Zhang, T.; Xu, X.; Li, Y.; Lv, X. The function of Cr on the rust formed on weathering steel performed in a simulated tropical marine atmosphere environment. *Constr. Build. Mater.* **2021**, *277*, 122298. [CrossRef]
4. Banaś, J.; Górecki, W.; Kurzydłowski, K.; Mazurkiewicz, B.; Pawlikowski, M.; Rożniatowski, K.; Solarski, W. *Research in Polish Metallurgy at the Beginning of XXI Century*; Świątkowski, K., Ed.; Publishing House "Akapit": Kraków, Poland, 2006.
5. Banaś, J.; Lelek-Borkowska, U.; Mazurkiewicz, B.; Solarski, W. Effect of CO_2 and H_2S on the composition and stability of passive film on iron alloys in geothermal water. *Electrochim. Acta* **2007**, *52*, 5704–5714. [CrossRef]
6. Banaś, J.; Pawlikowski, M.; Górecki, W.; Kurzydłowski, K. *Atlas of Geothermal Mesosoic Formation at Polish Lowland*; Górecki, W., Ed.; AGH: Kraków, Poland, 2006.
7. Łukaszczyk, A.; Mazurkiewicz, B.; Solarski, W.; Banaś, J. Wpływ CO_2 oraz temperatury na własności anodowe żelaza w wodzie termalnej. *Ochr. Przed Korozją* **2006**, *49*, 203–207.
8. Banaś, J.; Mazurkiewicz, B.; Solarski, W. Elektrochemiczne badania korozyjne w instalacjach geotermalnych. *Przegląd Geol.* **2009**, *57*, 664–666.
9. Ueda, M.; Ikeda, A. Effect of microstructure and Cr content in steel on CO_2 corrosion. In Proceedings of the Corrosion 96 Conference, Denver, CO, USA, 24–29 March 1996. Paper 13.
10. Hua, Y.; Mohammed, S.; Barker, R.; Neville, A. Comparisons of corrosion behaviour for X65 and low Cr steels in high pressure CO_2-saturated brine. *J. Mater. Sci. Technol.* **2020**, *41*, 21–32. [CrossRef]
11. Banaś, J.; Łukaszczyk, A.; Mazurkiewicz, B.; Solarski, W. Mechanizm i kinetyka korozji w układzie H_2O-NaCl-CO_2-H2S. Badania w warunkach laboratoryjnych i w polskich instalacjach geotermalnych. *Ochr. Przed Korozją* **2010**, *3*, 94–105.
12. Hedayat, A.; Yannacopoulos, S.; Postlethwaite, J. Wear and CO_2 corrosion of steel couplings and tubing in heavy oil screw-pump wells. *Wear* **1997**, *209*, 263–273. [CrossRef]
13. Cheng, Y.F.; Steward, F.R. Corrosion of carbon steels in high-temperature water studied by electrochemical techniques. *Corros. Sci.* **2004**, *46*, 2405–2420. [CrossRef]
14. Xu, L.; Wang, B.; Zhu, J.; Li, W.; Zheng, Z. Effect of Cr content on the corrosion performance of low-Cr alloy steel in a CO_2 environment. *Appl. Surf. Sci.* **2016**, *379*, 39–46. [CrossRef]
15. Sun, B.; Zuo, X.; Cheng, X.; Li, X. The role of chromium content in the long-term atmospheric corrosion process. *NPJ Mater. Degrad.* **2020**, *4*, 37. [CrossRef]
16. Sun, J.; Sun, C.; Wang, Y. Effect of Cr Content on the Electrochemical Behavior of Low chromium X65 Steel in CO_2 Environment. *Int. J. Electrochem. Sci.* **2016**, *11*, 8599–8611. [CrossRef]
17. Hamm, D.; Olsson, C.O.A.; Landolt, D. Effect of chromium content and sweep rate on passive film growth on iron–chromium alloys studied by EQCM and XPS. *Corros. Sci.* **2002**, *44*, 1009–1025. [CrossRef]
18. Hubschmid, C.; Landolt, D.; Mathieu, H.J. XPS and AES analysis of passive films on Fe-25Cr-X (X = Mo, V, Si and Nb) model alloys. *J. Anal. Chem.* **1995**, *353*, 234–239.
19. Kolotyrkin, Y.M. *Stress Corrosion Cracking and Hydrogen Embrittlement of Iron Base Alloys*; National Association of Corrosion Engineers: Houston, TX, USA, 1977; p. 946.
20. Lizlovs, E.A.; Bond, A.P. Anodic polarization behavior of high purity 13 and 18% cr stainless steels. *J. Electrochem. Soc.* **1975**, *122*, 719–722. [CrossRef]
21. Marcus, P. The role of alloyed elements and adsorbed impurities in passivation of metal-surfaces. *J. Chim. Phys.* **1991**, *88*, 1697–1711. [CrossRef]
22. Yang, W.P.; Costa, D.; Marcus, P. Chemical Composition, Chemical states, and resistance to localized corrosion of passive films on an Fe-17%Cr alloy. *J. Electrochem. Soc.* **1994**, *141*, 111–116. [CrossRef]

23. Massoud, T.; Maurice, V.; Klein, L.H.; Marcus, P. Nanoscale morphology and atomic structure of passive films on stainless steel. *J. Electrochem. Soc.* **2013**, *160*, C232–C238. [CrossRef]

24. Monnartz, P. Beitrag zum Studium der Eisenchromlegierungen unter besonderer Berücksichtigung der Säurebeständigkeit. *Metallurgie* **1911**, *8*, 161–170, 193–201.

25. Diawara, B.; Beh, Y.A.; Marcus, P. Nucleation and growth of oxide layers on stainless steels (FeCr) using a virtual oxide layer model. *J. Phys. Chem. C* **2010**, *114*, 19299–19307. [CrossRef]

26. Legrand, M.; Diawara, B.; Legendre, J.J.; Marcus, P. Three-dimensional modelling of selective dissolution and passivation of iron–chromium alloys. *Corros. Soc.* **2002**, *44*, 773–790. [CrossRef]

27. Diawara, B.; Legrand, M.; Legendre, J.J.; Marcus, P. Use of quantum chemistry results in 3D modeling of corrosion of iron-chromium alloys. *J. Electrochem. Soc.* **2004**, *151*, B172–B178. [CrossRef]

28. Keller, P.; Strehblow, H.H. XPS investigations of electrochemically formed passive layers on Fe/Cr-alloys in 0.5 M H_2SO_4. *Corros. Sci.* **2004**, *46*, 1939–1952. [CrossRef]

29. Inaba, H.; Kimura, M.; Yokokawa, H. An analysis of the corrosion resistance of low chromium-steel in a wet CO_2 environment by the use of an electrochemical potential diagram. *Corros. Sci.* **1996**, *38*, 1449–1461. [CrossRef]

30. Marcus, P. Surface science approach of corrosion phenomena. *Electrochim. Acta* **1998**, *43*, 109–118. [CrossRef]

31. Heusler, K.E.; Kusian, B.; MCPhail, D. Kinetics of the Corrosion of Iron in Aqueous Electrolytes at Temperatures up to 300 °C. *Ber. Bunsenges. Phys. Chem.* **1990**, *94*, 1443–1449. [CrossRef]

32. Sato, N.; Kudo, K.; Noda, T. The anodic oxide film on iron in neutral solution. *Electrochim. Acta* **1971**, *16*, 1909–1921. [CrossRef]

33. Sato, N.; Kudo, K.; Nishimura, R. Depth Analysis of Passive Films on Iron in Neutral Borate Solution. *J. Electrochem. Soc.* **1976**, *123*, 1419–1423. [CrossRef]

34. Bessone, J.; Karakaya, L.; Lorbeer, P.; Lorenc, W.J. The kinetics of iron dissolution and passivation. *Electrochim. Acta* **1977**, *22*, 1147–1154. [CrossRef]

35. Bard, A.; Faulkner, L. *Electrochemical Methods: Fundamentals and Applications*; John Wiley & Sons: New York, NY, USA, 2001.

36. Laviron, E. General expression of the linear potential sweep voltammogram in the case of diffusionless electrochemical systems. *J. Electroanal Chem.* **1979**, *101*, 19–28. [CrossRef]

37. Lorenz, W.J.; Heusler, K.E. *Corrosion Mechanisms*; Mansfeld, F., Dekker, M., Eds.; Wiley: New York, NY, USA, 1987.

38. Langmuir, I. The pressure effect and other phenomena in gaseous discharges. *J. Frankl. Inst.* **1923**, *196*, 751–762. [CrossRef]

39. Deroubaix, G.; Marcus, P. X-ray photoelectron spectroscopy analysis of copper and zinc oxides and sulphides. *Surf. Interface Anal.* **1992**, *18*, 39–46. [CrossRef]

40. Barr, T.L.; Hackenberg, J.J. Studies of the low temperature oxidation of alloys by X-ray photoelectron spectroscopy: Cu–Zn. *Appl. Surf. Sci.* **1982**, *10*, 523–545. [CrossRef]

41. Dake, L.S.; Baer, D.R.; Zachara, J.M. Auger parameter measurements of zinc compounds relevant to zinc transport in the environment. *Surf. Interface Anal.* **1989**, *14*, 71–75. [CrossRef]

42. Beamson, G.; Briggs, M.D. *High. Resolution XPS Spectra of Organic Polymers*; Wiley: New York, NY, USA, 1992.

43. Mohapatra, J.N.; Panda, A.K.; Gunjan, M.K.; Bandyopadhyay, N.R.; Mitra, A.; Ghosh, R.N. Ageing behavior study of 5Cr–0.5 Mo steel by magnetic Barkhausen emissions and magnetic hysteresis loop techniques. *NDTE Int.* **2007**, *40*, 173–178. [CrossRef]

44. Gupta, R.P.; Sen, S.K. Calculation of multiplet structure of core p-vacancy levels. *Phys. Rev. B* **1974**, *10*, 71–77. [CrossRef]

45. Gupta, R.P.; Sen, S.K. Calculation of multiplet structure of core p-vacancy levels. II. *Phys. Rev. B* **1975**, *12*, 15–19. [CrossRef]

46. Grosvenor, A.P.; Kobe, B.A.; Biesinger, M.C.; McIntyre, N.S. Investigation of multiplet splitting of Fe 2p XPS spectra and bonding in iron compounds. *Surf. Interface Anal.* **2004**, *36*, 1564–1574. [CrossRef]

47. Furlani, A.; Russo, M.V.; Polzonetti, G.; Martin, K.; Wang, H.H.; Ferraro, J.R. Spectroscopic studies of $FeCl_3$-doped polymers of polyphenylacetylene. *Appl. Spectrosc.* **1990**, *44*, 331–334. [CrossRef]

48. Maurice, V.; Cadot, S.; Marcus, P. Hydroxylation of ultra-thin films of α-Cr_2O_3(0001) formed on Cr(110). *Surf. Sci.* **2001**, *471*, 43–58. [CrossRef]

49. Oku, M.; Suzuki, S.; Ohtsu, N.; Shishido, T.; Wagatsuma, K. Comparison of intrinsic zero-energy loss and Shirley-type background corrected profiles of XPS spectra for quantitative surface analysis: Study of Cr, Mn, and Fe oxides. *Appl. Surf. Sci.* **2008**, *254*, 5141–5148. [CrossRef]

50. Pratt, A.R.; McIntyre, N.S. Comment on 'curve fitting of Cr 2p photoelectron spectra of Cr_2O_3 and CrF_3. *Surf. Interface Anal.* **1996**, *24*, 529–530. [CrossRef]

51. Chambers, S.A.; Droubay, T. Role of oxide ionicity in electronic screening at oxide/metal interfaces. *Phys. Rev. B* **2001**, *64*, 075410. [CrossRef]

52. Ünveren, E.; Kemnitz, E.; Hutton, S.; Lippitz, A.; Unger, W.E.S. Analysis of highly resolved x-ray photoelectron Cr 2p spectra obtained with a Cr_2O_3 powder sample prepared with adhesive tape. *Surf. Interface Anal.* **2004**, *36*, 92–95. [CrossRef]

53. Asami, K.; Hashimoto, K. An XPS study of the passivity of a series of iron- chromium alloys in sulfuric acid. *Corros. Sci.* **1978**, *18*, 151–160. [CrossRef]

54. Brüesch, P.; Müller, M.; Atrens, A.; Neff, H. Corrosion of stainless steels in chloride solution: An XPS investigation of passive films. *Appl. Phys. A* **1985**, *38*, 1–18. [CrossRef]

55. Kirchheim, R.; Heine, B.; Fischmeister, H.; Hofmann, S.; Knote, H.; Stolz, U. The passivity of iron-chromium alloys. *Corros. Sci.* **1989**, *29*, 899–917. [CrossRef]